Materials Horizons

COMMUNICATION

View Article Online
View Journal

Cite this: DOI: 10.1039/d5mh02144h

Received 11th November 2025,
Accepted 19th March 2026

DOI: 10.1039/d5mh02144h

rsc.li/materials-horizons

# High-performance transparent metal mesh electrodes utilizing a metal-vapor-desorption layer for organic light-emitting diode applications

Dahyun Kim,[ab] Sujin Jeong,[ab] Dong Keon Lee,[ab] Wonjune Yi,[ab] Hyungsoo Yoon,[ab] Joohee Jeon,[ab] Hayun Kim,[ab] Byeongmoon Lee*[c] and Yongtaek Hong*[ab]

**Transparent conducting electrodes (TCEs) are essential for high-performance organic light-emitting diodes (OLEDs), particularly in transparent and flexible device architectures. Conventional TCEs such as indium tin oxide (ITO) suffer from mechanical brittleness and limited material availability, and often require sputtering processes that can damage underlying organic layers. In response, various alternatives including conductive polymers and nanomaterials or structure-based approaches of metallic films have been explored. However, many of these approaches still face limitations such as low conductivity, poor interfacial contact, or solvent compatibility issues that may degrade device performance. To overcome these challenges, we present a novel direct patterning strategy for top transparent metal mesh electrodes using the metal desorption behavior of solution-processed poly(vinylidene fluoride-*co*-hexafluoropropylene) (PVDF–HFP) and a transfer printing method. By thermally evaporating silver onto patterned PVDF–HFP layers, we successfully fabricated metal mesh electrodes with high optical transmittance, low sheet resistance, and a maximum figure of merit exceeding 10$^4$ using the ratio of electrical conductivity to optical conductivity, which is among the highest reported for sub-micrometer transparent electrodes. This method does not require any lamination, or immersion in solvents or electrolytes, enabling direct integration onto sensitive organic layers. With improved transparency, the metal mesh electrodes were able to be applied as the top cathodes of OLEDs exhibiting comparable electroluminescence characteristics to those with conventional electrodes.**

### New concepts

We report a simple, maskless and damage-free strategy to realize high-performance transparent metal mesh electrodes directly on "organic layers" of organic light-emitting diodes (OLEDs). Conventional transparent electrodes often fail to combine high optical transmittance and excellent electrical performance with device-compatible fabrication processes; methods fulfilling all these requirements have not yet been reported. Our concept exploits the transfer-printed metal-vapor-desorption layer based on an elastomeric fluoropolymer that efficiently repels incoming metal vapor during thermal evaporation. Unlike previously reported high-performance transparent metal meshes that involve chemical washing steps, our method enables high-fidelity transparent metal mesh patterns without chemical washing or lift-off, maintaining the integrity of underlying devices. Achieving a high optical transparency (93–99%) and an ultra-low sheet resistance (1.1–4.0 Ohm sq$^{-1}$), the resulting silver mesh electrodes exhibit an exceptional figure of merit exceeding 10$^4$, which, to the best of our knowledge, is the highest value among sub-micrometer-thick transparent electrodes. As a proof of concept, we for the first time fabricated transparent OLEDs using transparent metal mesh top cathodes, demonstrating enhanced transparency and current efficiency without device degradation. This approach provides a practical route to integrate high-performance transparent electrodes with organic devices, offering a universal platform for next-generation transparent electronics and display technologies.

## 1. Introduction

Organic light-emitting diodes (OLEDs) have been extensively studied for their potential in transparent and flexible thin-film display applications.[1,2] To efficiently extract the light generated inside the light-emitting devices, OLEDs inevitably require a transparent electrode on the top and/or bottom, depending on the intended emission direction. The development of transparent conducting electrodes (TCEs) for light-emitting devices relies on high optical transmittance and low sheet resistance.[3,4] In addition, electrode properties can further influence the device characteristics of OLEDs, and therefore various TCEs have been implemented in OLEDs to evaluate their impact on performance metrics such as external quantum efficiency and efficiency roll-off.[5–7]

---

[a] *Department of Electrical and Computer Engineering, Seoul National University, Seoul 08826, Korea. E-mail: yongtaek@snu.ac.kr*

[b] *Inter-university Semiconductor Research Center (ISRC), Seoul National University, Seoul 08826, Korea*

[c] *Department of Electrical Engineering and Computer Science, Daegu Gyeongbuk Institute of Science and Technology (DGIST), Daegu 42988, Korea. E-mail: byeongmoon@dgist.ac.kr*

A typical approach to developing TCEs involves the use of transparent conductive oxides, especially indium tin oxide (ITO),[4,8–11] which suffers from inherent brittleness and low material abundance.[3] Furthermore, the underlying organic layers can be damaged during ITO sputtering.[12] Various alternatives to ITO have been investigated, including material-based or structure-based approaches. For material-based approaches, conductive polymers[6,13] or novel nanomaterials such as metal nanowires,[7,14] graphene,[15,16] or carbon nanotubes (CNTs)[17] were suggested, but they exhibit limited performance (*i.e.*, figure of merit) for TCEs due to their intrinsically low electrical conductivity.

Beyond material-based alternatives, structure-based approaches have been actively explored to overcome the fundamental trade-off between transparency and conductivity in TCEs. One typical approach is to reduce the thickness of the deposited metal to a scale of several nanometers. Thermally evaporated metal layers offer high purity films and excellent electrical conductivity. Therefore, thermally evaporated ultrathin metallic films can achieve reasonable transparency with high electrical conductivity. Nevertheless, ultrathin metallic films inherently suffer from limited transparency due to strong optical absorption and island type growth of metals.[3,18] To overcome this limitation of low transparency, additional dielectric layers in dielectric/metal/dielectric (D/M/D) multilayers have been suggested to improve the overall transparency using optical interference or surface plasmonic effects.[2,19–21] However, the introduction of additional dielectric layers leads to complicated fabrication processes and often induces mechanical brittleness, limiting applicability in flexible electronics.

Other structure-based methods include the patterning of metallic films, resulting in a high open-area ratio (*i.e.*, a low fill factor), which can significantly enhance transmittance while maintaining the conductive properties of metallic films.[22,23] Metallic films can be patterned *via* printing methods using conductive metallic ink, including inkjet printing[24] and roll-to-roll processing.[25–27] While printing of conductive metallic inks enables the realization of arbitrarily shaped patterns with substantial design freedom, the presence of residual solvents still poses a risk of degradation to the underlying layers.[28] Employing orthogonal solvents or introducing an effective buffer layer can help mitigate issues arising from solvent penetration. However, printed metal films generally have inferior film integrity compared to evaporated metal films, exhibiting limited electrical conductivity.[29] Therefore, evaporated metal meshes have been considered an attractive approach to achieve highly conductive transparent metallic films.

Patterning of evaporated metal films can be generally achieved by using shadow masks or photolithography. While shadow masks offer a simple method for patterning metals without damaging underlying devices, they are limited in their ability to define patterns with internal holes, including mesh or grid structures. On the other hand, photolithography can be applied to pattern metal films without this limitation. However, photolithography involves solvent rinsing steps[30,31] or UV exposure, which may degrade the underlying device layers.[32] Thus, these constraints make the direct fabrication of top transparent mesh electrodes on OLEDs highly challenging. Moreover, electrodeposition can further increase the thickness of photolithography-based patterns, achieving metal mesh patterns with extremely improved electrical performance.[33,34] However, electrodeposition generally requires immersing the entire substrate into an electrolyte solution, making it incompatible with pre-fabricated OLEDs containing sensitive organic layers and thus limiting its direct application to such devices. Therefore, a precise patterning method for highly conductive, high-performance TCEs without affecting the underlying delicate organic layers is still needed.

To overcome the limitations of previous methods for TCEs on optoelectronic devices, alternative approaches have been suggested. Interestingly, several studies have reported materials with desorption effects that can repel incoming metal vapor during vacuum thermal evaporation. Fluorinated polymers,[35–38] photochromic diarylethene,[39–42] and evaporated organic materials[43,44] were reported for this desorption behavior. By utilizing these desorption layers, metal films can be patterned exclusively in the desired regions with high-resolution and excellent fidelity. However, previous approaches for desorption-based transparent electrodes mostly include an additional chemical rinsing step, to achieve low absorption and better transmittance, by removing the metal nanoparticles deposited on the desorption material. Solvent rinsing may adversely affect the integrity of the predeposited organic layers, depending on the devices. Therefore, it is highly desirable to develop a method for fabricating high-performance, highly transparent electrodes without any additional chemical treatment, particularly for silver, a widely used conductive metal in electronic devices.

In this study, we report the patterning of the transparent top metal mesh electrodes on OLEDs *via* selective metal deposition guided by the desorption behavior of elastomeric poly(vinylidene fluoride-*co*-hexafluoropropylene) (PVDF–HFP). This process fully utilizes the excellent metal desorption characteristics of this printable ink, which eliminates the need for solvent rinsing to remove residual metal nanoparticles. Furthermore, by introducing the transfer printing method of spin-coated metal desorption patterns with minimized solvent, our method simultaneously enables high-resolution mesh patterns with high fidelity while avoiding adverse effects of residual ink solvents on the underlying organic device layers. Although directly printed ink patterns inevitably involve solvent contact with the target surface, which could penetrate the underlying organic layer stacks, the proposed solvent-minimized transfer printing allows the metal vapor desorption layer to be delivered as a film with minimal solvent exposure at the target surface. Despite employing relatively thick Ag films (100–300 nm), the resulting patterned electrodes exhibit excellent optical transparency (93.6–99.0%) and a low sheet resistance (1.1–4.4 Ohm sq$^{-1}$), achieving a figure of merit exceeding $10^4$ at 200 nm thickness, one of the highest reported among transparent electrodes with sub-micrometer thickness. The resulting metal mesh electrodes can be directly applied on top of the organic optoelectronic devices. To the best of our knowledge, this is the first reported direct integration of transparent metal mesh top electrodes onto OLEDs without any lamination processes or buffer layers, enabling versatile integration into organic optoelectronic devices.

## 2. Results and discussion

### 2.1. Metal mesh electrode patterned by selective deposition

Fig. 1 illustrates the concept of a transparent metal mesh electrode being directly fabricated on top of organic light-emitting diodes (OLEDs). The fabrication process for a metal mesh electrode involves the following processes: (1) transfer printing of an array-patterned metal-vapor-desorption layer and (2) selective metal deposition enabled by the desorption characteristics of elastomeric PVDF–HFP. The molar ratio of vinylidene fluoride (VDF) and hexafluoropropylene (HFP) was calculated from the known fluorine content (66 mass%), revealing a relatively high HFP content of 22 molar%. This high HFP content enhances the elastomeric properties of the copolymer compared to crystalline PVDF–HFP, making it suitable for exhibiting desorption behavior.[38,42] Following our previous work,[38] the metal-vapor-desorption layer ink (e-PVDF–HFP ink) was prepared by dissolving elastomeric PVDF–HFP and cross-linking agents in propylene glycol monomethyl ether acetate (PGMEA). The square array-patterned metal-vapor-desorption layer was achieved by transfer printing of the e-PVDF–HFP films using a PDMS micropillar stamp. For metal deposition, silver (Ag) was deposited *via* thermal evaporation under high vacuum conditions ($<10^{-6}$ torr). During metal deposition onto the patterned e-PVDF–HFP film, the formation of continuous Ag films was inhibited on the regions with the e-PVDF–HFP film by repelling the Ag vapor, although Ag films were successfully formed on the regions without the e-PVDF–HFP film. Accordingly, as shown in Fig. 1b, self-aligned metal mesh patterning was demonstrated *via* selective metal deposition on both bare substrate and OLED devices without complex lithographic processes.

Fig. 1c shows a photograph of the fabricated metal mesh electrode on a glass substrate placed over a background image to demonstrate its visual transparency, along with the optical microscopy and high-resolution field-emission scanning electron microscopy (FE-SEM) images that confirm the formation of well-defined mesh patterns. Also, due to its excellent compatibility with the underlying organic devices, a self-aligned metal mesh electrode was directly fabricated as the top electrode on a transparent OLED device. Fig. 1d shows an electroluminescence (EL) emission photograph of the fabricated transparent OLED with a top metal mesh electrode. These results demonstrate that the Ag top electrode was effectively patterned on the OLED device without damaging the underlying organic layers. Notably, this process requires no additional buffer layer or lamination step. These directly fabricated metal mesh electrodes can fully utilize the existing deposition materials and methods for conventional OLED fabrication, enabling simplified fabrication without the need for complex processing steps.

### 2.2. Fabrication of self-aligned metal mesh electrodes

Fig. 2 illustrates the fabrication process of metal mesh (Fig. 2a), and the following self-aligned selective deposition (Fig. 2b). The overall process consists of four main steps, which are (i) fabrication of the PDMS micropillar stamp, (ii) stamp coating,

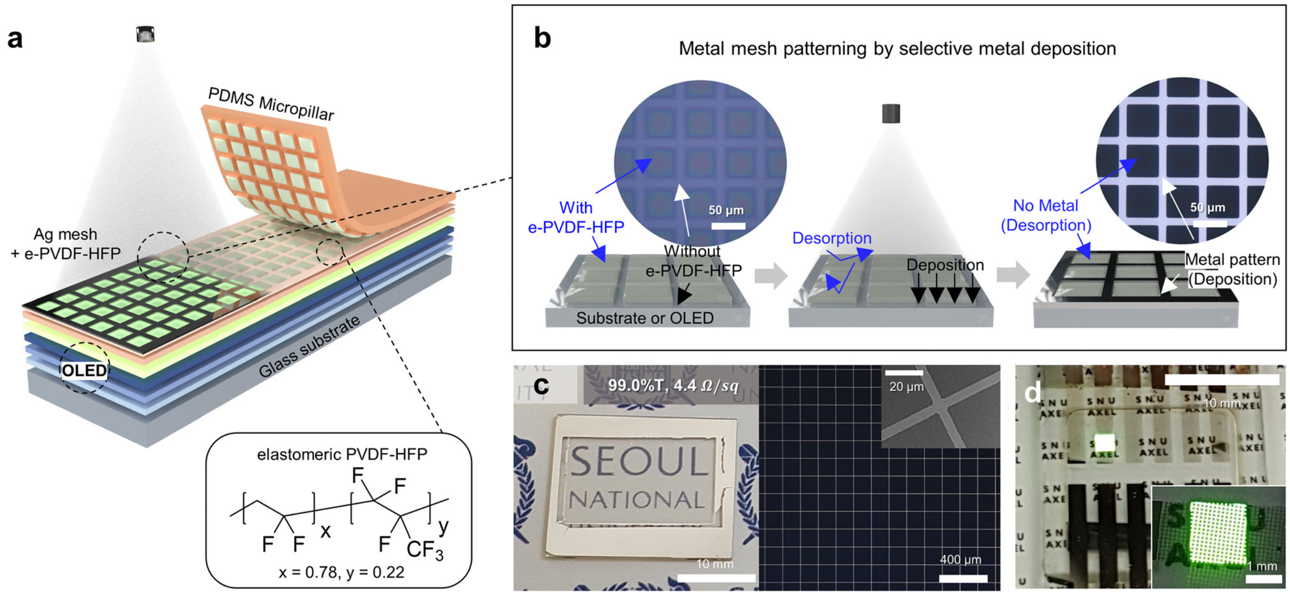

Fig. 1 (a) Graphical concept image of a transparent OLED with a selectively deposited metal mesh top electrode using a micro-contact printed metal-vapor-desorption layer pattern (inset: main material of the metal-vapor-desorption layer ink, elastomeric poly(vinylidene fluoride-*co*-hexafluoropropylene) (elastomeric PVDF–HFP)). (b) Self-aligned metal mesh patterning using desorption characteristics (inset: optical microscopic image of the patterned e-PVDF–HFP film on the glass substrate before and after selective metal deposition). (c) Optical image and SEM image of an example transparent electrode. (d) Emission image of a transparent OLED with a metal mesh top electrode.

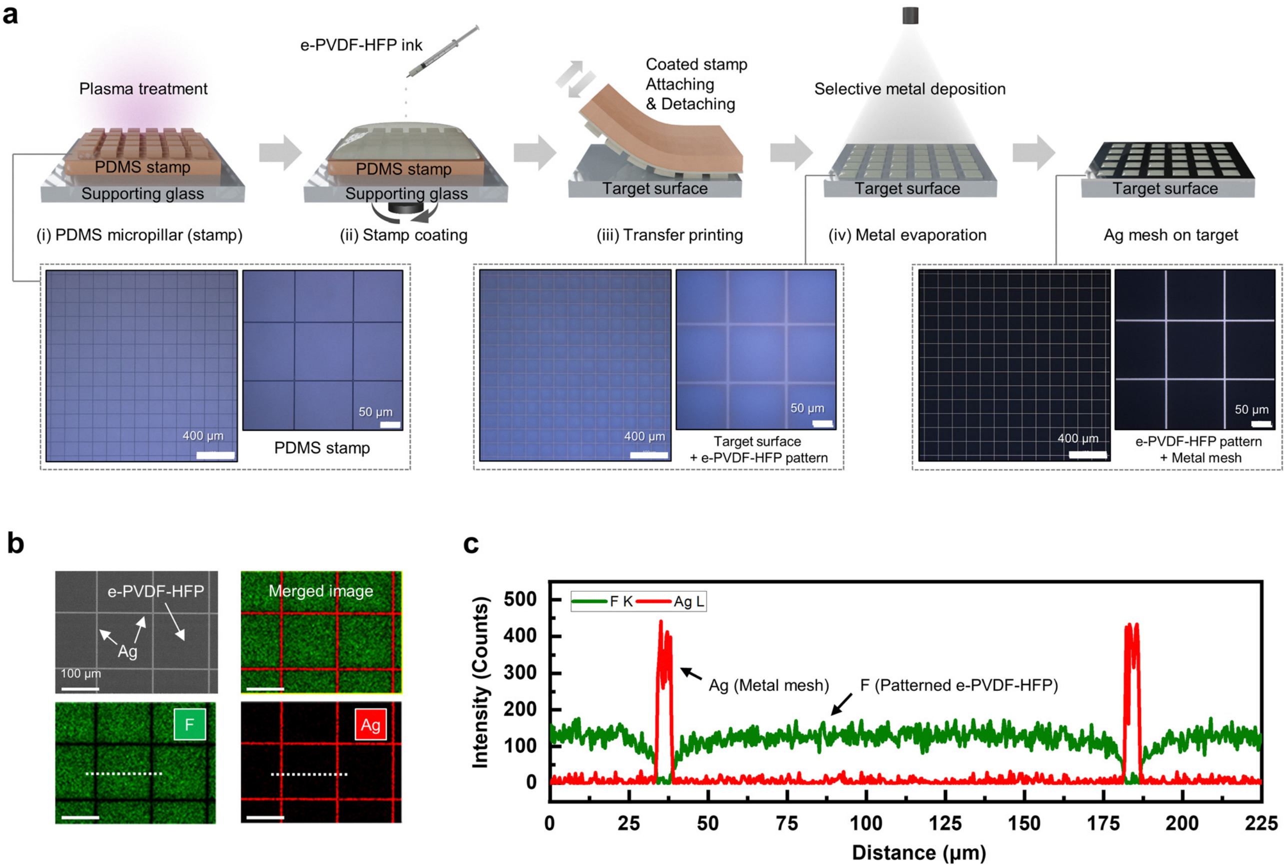

Fig. 2 Self-aligned metal mesh patterning process of the metal mesh electrode. (a) Fabrication process, (b) SEM-EDS mapping of the fabricated mesh patterned Ag electrode, and (c) EDS line scan analysis of the fabricated Ag mesh electrode.

(iii) transfer printing, and (iv) metal evaporation. Specifically, a polydimethylsiloxane (PDMS) mixture was poured onto the pre-patterned silicon (Si) wafer treated with an anti-adhesion agent, trichloro(1*H*,1*H*,2*H*,2*H*-perfluorooctyl)silane (FOTS).[45] After spin-coating, the PDMS micropillar stamp was peeled off from the master mold. Here, the PDMS micropillar stamps with different pillar dimensions were used, including pillar widths of 46.8 μm, 66.4 μm, 95.9 μm, and 143.2 μm, and pillar array spacings of 12 μm, 7.4 μm, 4.7 μm, and 3.6 μm, with a pillar height of 8 μm. To enhance the wettability, the PDMS micropillar stamp was treated with air plasma at an optimized power before coating. Plasma treatment is a widely used surface modification method that introduces silanol groups (–OH) instead of methyl groups ($-CH_3$), resulting in a more hydrophilic surface.[46] Stamp coating was carried out by spin-coating the e-PVDF–HFP ink, and the e-PVDF–HFP pattern was transfer printed onto the target surface. With the optimized plasma treatment conditions applied to the PDMS micropillar stamp, the spin-coated e-PVDF–HFP was transferred onto the target substrate in various widths of desired patterns (Fig. S1 and Table S1), closely replicating the original pattern of the PDMS micropillar stamp, as shown in the inset of Fig. 2a.

After evaporation, metal film was selectively deposited in regions without the e-PVDF–HFP film, resulting in a metal mesh with a square grid pattern complementary to the array-patterned e-PVDF–HFP film. To confirm, the fabricated metal mesh was analyzed using field-emission scanning electron microscopy (FE-SEM) and energy-dispersive X-ray spectroscopy (EDS) mapping (Fig. 2b). The SEM image shows that the array-patterned e-PVDF–HFP film and the complementary grid-patterned Ag mesh do not overlap, demonstrating successful selective metal deposition enabled by the desorption characteristics of the e-PVDF–HFP film. The EDS mapping image results and corresponding line scan analysis (Fig. 2c) further confirm the selective metal deposition, as Ag was detected exclusively in the region without the fluorine (F) signal originating from the e-PVDF–HFP. In addition, atomic force microscopy (AFM) analysis confirmed that Ag deposition does not induce significant morphological changes in the e-PVDF–HFP regions, except for localized Ag clustering or nanoparticle island formations (see Fig. S2 and S3).

### 2.3. Plasma treatment optimization for high fidelity transfer printing

Air plasma treatment was used to modify the surface energy of the hydrophobic PDMS surface into a hydrophilic surface. Here, plasma treatment effectively enhanced ink spreading on the PDMS micropillar stamp, during spin-coating, as illustrated in Fig. 3a. At low plasma treatment levels, the patterned e-PVDF–HFP film does not fully cover the PDMS micropillar stamp after spin-coating, and the transfer-printed e-PVDF–HFP film does not follow the designed stamp pattern, resulting in broader mesh linewidths. With sufficient plasma treatment, the patterned e-PVDF–HFP film can fully cover the PDMS micropillar stamp after spin-coating, resulting in the e-PVDF–HFP film with the designed pattern being transferred.

To analyze the effect of altering plasma treatment, under varying plasma treatment powers at a fixed plasma treatment time (30 s), surface wettability was compared *via* sessile drop contact angle measurement using the ink as a test liquid and the plasma-treated PDMS micropillar stamp as a test surface. As shown in Fig. 3b, the ink contact angle on plasma-treated PDMS micropillar stamps decreased with increasing plasma treatment power. Based on these contact angle measurements, the work of adhesion was also evaluated, revealing an increase with increasing plasma treatment power. Furthermore, after transfer printing, even with an identical PDMS micropillar stamp, the resulting pattern spacing varied with the plasma treatment power. The transferred e-PVDF–HFP patterns became more identical to the PDMS micropillar patterns with sufficient plasma treatment due to enhanced wettability, allowing the desorption layer areal coverage of the resulting metal mesh to closely match the designed geometrical transmittance. Desorption layer areal coverage was extracted from the optical images of the e-PVDF–HFP patterns.

On the other hand, excessive plasma treatment resulted in a distorted e-PVDF–HFP pattern after transfer, as shown in Fig. 3c. At high plasma treatment levels (100 W), the adhesion between the e-PVDF–HFP film and the PDMS stamp became

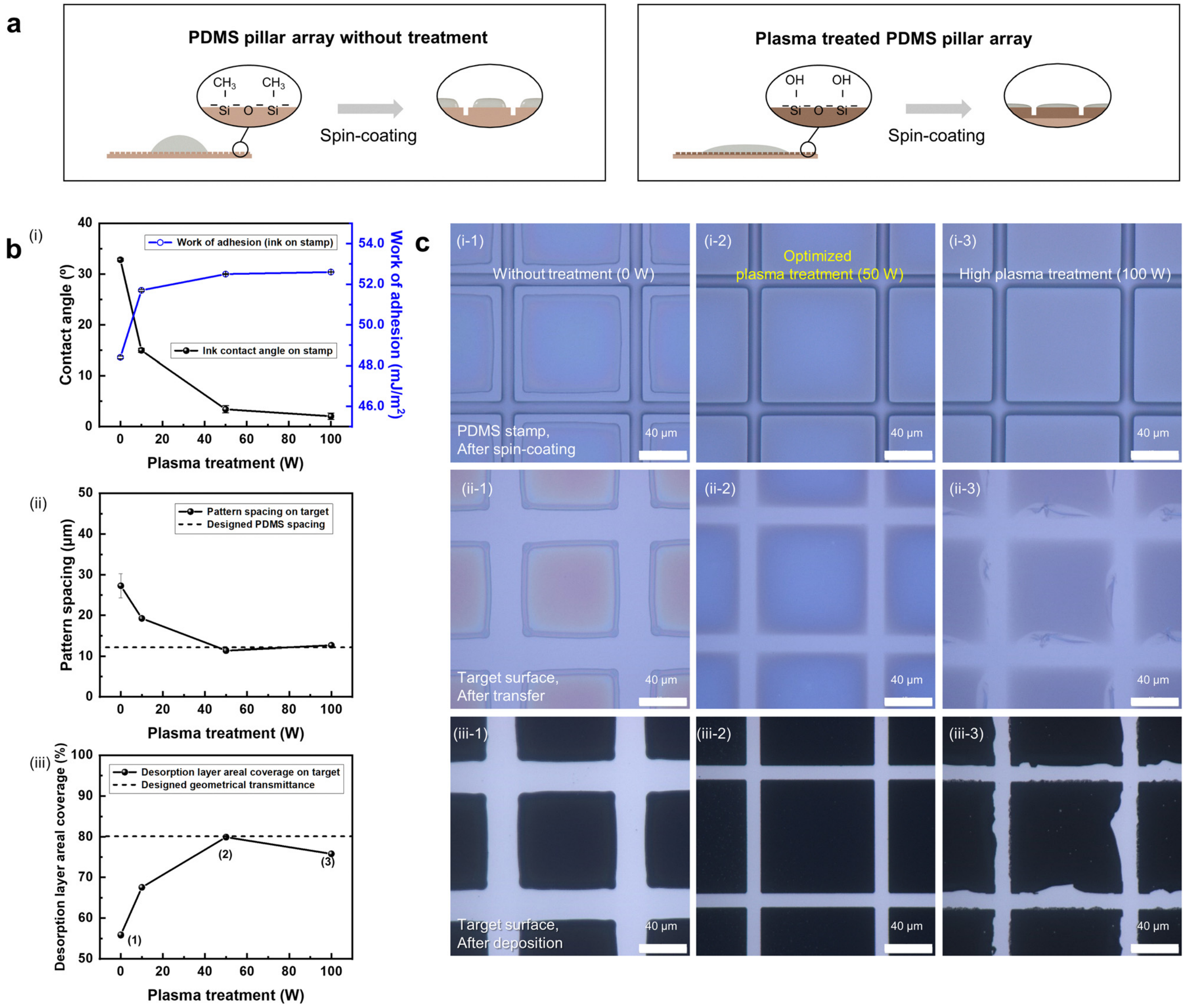

Fig. 3 Elastomeric PVDF–HFP patterning by spin-coating on the PDMS pillar array and consecutive transfer printing. (a) Schematic image representing surface plasma treatment on the PDMS pillar array, before and after spin-coating. (b) Wettability control *via* plasma treatment: (i) ink contact angle on the PDMS pillar array and the corresponding work of adhesion of the ink to the stamp, (ii) transferred pattern spacing on the target glass substrate, and (iii) the resulting desorption layer areal coverage on the target depending on plasma treatment. (c) Optical image of the spin-coated elastomeric PVDF–HFP pattern on the PDMS pillar array depending on plasma treatment power (i) before and (ii) after transfer onto the target substrate or (iii) after metallization. The plasma treatment time was fixed to 30 s for (b) and (c).

excessive, making the adhesion between the ink and the target surface insufficient compared to that between the ink and the stamp. During the transfer printing process, this insufficiency leads to partial delamination of the patterned e-PVDF–HFP film from the target surface, causing pattern distortion. With optimized plasma treatment (50 W), the transferred e-PVDF–HFP pattern and the corresponding metal mesh pattern properly replicate the designed geometry without distortion. These differences in pattern fidelity can be observed clearly in the optical microscopy images after metal deposition.

### 2.4. Optoelectronic properties of the fabricated metal mesh

Using different pillar widths and pillar array spacings, metal mesh electrodes with different metal deposition thicknesses were fabricated. The structural parameters of the PDMS micropillar stamp and the corresponding e-PVDF–HFP film or mesh pattern that were used in this study are summarized in Fig. 4a. As shown in Fig. 4a(i), the terms pillar width ($w$), pillar array spacing ($s$), and pillar height ($h$) are used to describe the dimensions of the PDMS micropillar stamp. After transfer printing and metal deposition, Fig. 4a(ii) defines the mesh pattern parameters as linewidth ($L$), line spacing ($L_s$), and metal deposition thickness ($h_m$). The mesh pattern parameters ($L_s$ or $L$) were determined by the structural parameters of the PDMS stamp ($w$ or $s$).

To analyze the electrical and optical characteristics of the fabricated metal mesh, optical transmittance, electrical sheet resistance, optical haze and the figure of merit (FoM) as a transparent electrode were compared. The FoM was calculated using the following equation (eqn (1)[47]),

$$\mathrm{FoM} = \frac{\sigma_{\mathrm{dc}}}{\sigma_{\mathrm{opt}}} = \frac{188.5}{R_s\left(\frac{1}{\sqrt{T}} - 1\right)} \tag{1}$$

where $\sigma_{\mathrm{dc}}$, $\sigma_{\mathrm{opt}}$, $R_s$, and $T$ represent the electrical DC conductivity, optical conductivity, sheet resistance, and optical transmittance (measured at 550 nm) of the transparent electrode, respectively. A lower $R_s$ and higher $T$ result in a higher FoM, indicating better overall performance as a transparent electrode. Detailed descriptions about the theoretical analysis of the FoM are further provided in the SI (Fig. S4 and Supplementary Note S1).

Electrical and optical characteristics of metal mesh electrodes with varying $L$, $L_s$, and metal deposition thicknesses were

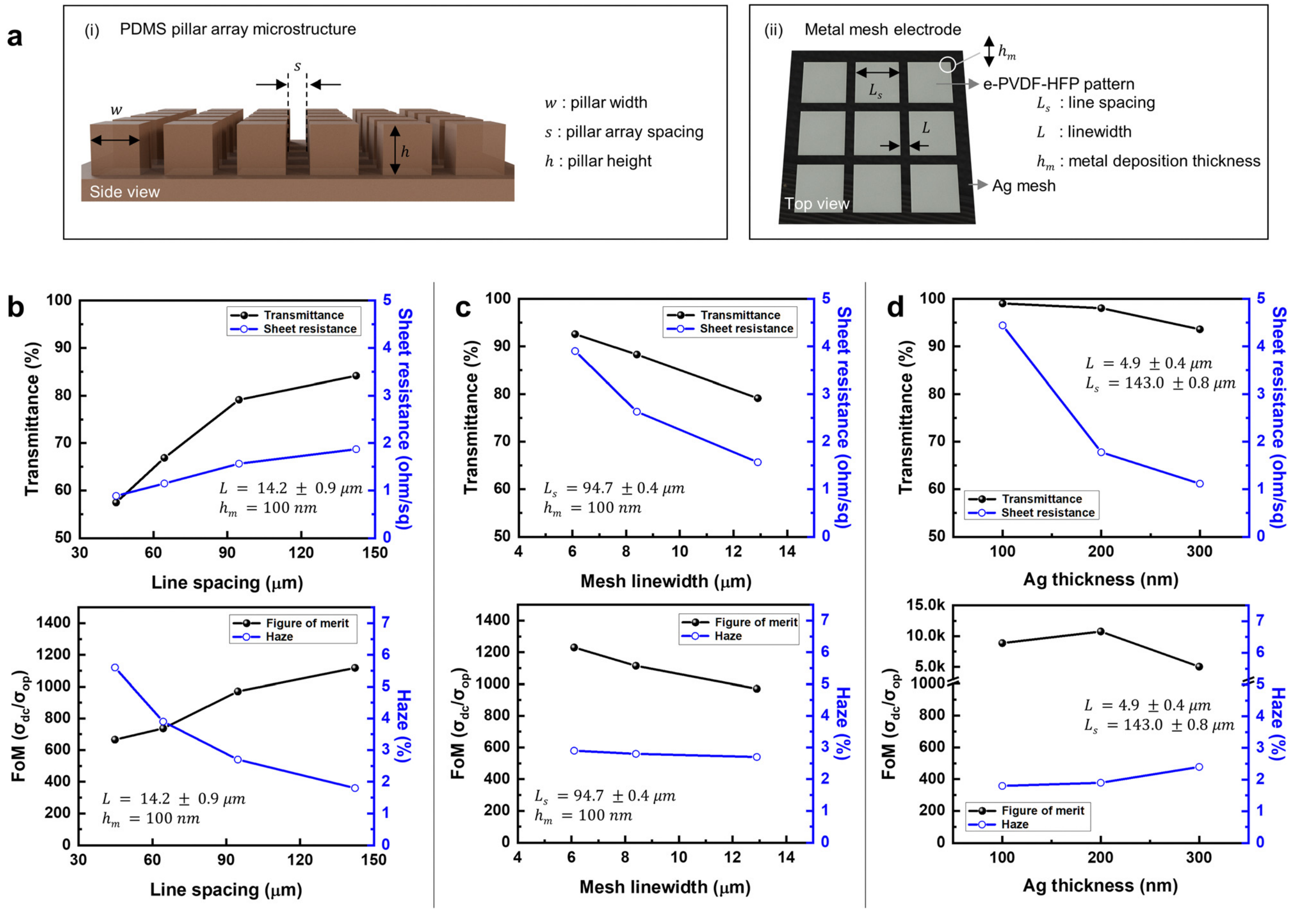

Fig. 4 (a) Schematic image representing geometrical parameters of (i) the PDMS pillar array microstructure and (ii) the metal mesh electrode. (b)–(d) Optical and electrical characteristics of the fabricated metal mesh (b) with different line spacing, (c) with different mesh linewidths, and (d) with different Ag thickness.

compared. Unless otherwise noted, the metal deposition thicknesses reported in this manuscript refer to the values monitored by the quartz crystal monitor. The thicknesses of the patterned metal films were further confirmed by surface profile measurements of the fabricated metal mesh electrodes after removing e-PVDF–HFP patterns by rinsing, as shown in the SI (Fig. S5). First, Fig. 4b shows the optical and electrical characteristics of metal mesh electrodes with varying $L_s$ of 44.8 μm, 64.4 μm, 94.7 μm, and 142.3 μm, with similar $L$ (14.2 ± 0.9 μm) and identical metal deposition thickness (100 nm). An increased $L_s$ leads to higher optical transmittance (57.5 to 84.2 %$T$) and elevated sheet resistance (0.887 to 1.87 Ohm sq$^{-1}$). Considering both optical and electrical properties, the FoM of the fabricated metal mesh improved from 666.0 to 1117.7 with increasing $L_s$. In addition, as $L_s$ increased, light scattering decreased, resulting in reduced optical haze (from 5.6 to 1.8%).

Then, metal meshes with varying $L$ of 12.9 μm, 8.4 μm, and 6.1 μm were fabricated (Fig. 4c) with similar $L_s$ (94.7 ± 0.4 μm) and identical metal deposition thickness (100 nm). As $L$ decreased, the optical transmittance improved (from 79.1 to 92.6 %$T$), while the sheet resistance increased (1.57 to 3.90 Ohm sq$^{-1}$). Although the FoM of the fabricated metal mesh improved with decreasing $L$ (from 970.3 to 1229.9), the optical haze slightly increased from 2.7% to 2.9% at smaller $L$, which can be attributed to increased light scattering in finer patterns.

Furthermore, the sheet resistance of the metal mesh was effectively reduced by increasing the metal deposition thickness from 100 nm to 300 nm, while maintaining similar $L_s$ (143.0 ± 0.8 μm) and $L$ (4.9 ± 0.4 μm). As shown in Fig. 4d, as the metal deposition thickness increased, the sheet resistance reduced from 4.44 to 1.11 Ohm sq$^{-1}$, while the optical transmittance slightly decreased from 99.0 to 93.6 %$T$. This reduction in transmittance, which can also be observed in non-patterned e-PVDF–HFP films (Fig. S6), is primarily attributed to a small amount of metal deposition on the desorption layer at higher deposition thickness (above 150 to 200 nm). SEM images confirmed the growth of Ag nanoparticle islands and clusters for different Ag deposition thicknesses, as shown in the SI (Fig. S3, S7, and S8). The optical haze also increased (1.8–2.4%) as the metal deposition thickness increased, due to increased optical scattering from those Ag nanoparticles. Overall, the FoM of the metal mesh was calculated to be 8866.4 (100 nm), 10 756.4 (200 nm), and 5038.1 (300 nm). Detailed data, optical microscopic images, and spectral transmittance data for each metal mesh are provided in the SI (Fig. S9–S11 and Tables S2–S4). As summarized in Fig. S12 and Table S5 (SI), compared to a reference commercial ITO-coated glass or non-patterned Ag films, the fabricated metal mesh electrodes exhibited lower or comparable sheet resistance and reached higher optical transmittance.

Additionally, Fig. 5a and Table S6 compare sheet resistance verses optical transmittance and the FoM of the fabricated metal mesh electrodes to those of various TCEs, including widely used transparent conducting oxides (ITO[8] or IZO[48]), ultrathin metal films,[49,50] D/M/D multilayers,[51,52] nanomaterials (silver nanowires (AgNWs),[7,14] graphene,[15] or CNTs[17]), and evaporated metal mesh[37,53] or printed metal mesh[24,26] reported in previous studies, especially with high transmittance and low sheet resistance. The maximum FoM of our evaporated metal mesh electrode was found to be 10 756.4, which surpasses those of other transparent electrodes. This result is attributed to our fabrication method, which simultaneously enables high-fidelity patterning and high-quality metal film deposition. Therefore, the proposed metal mesh electrodes can be an effective

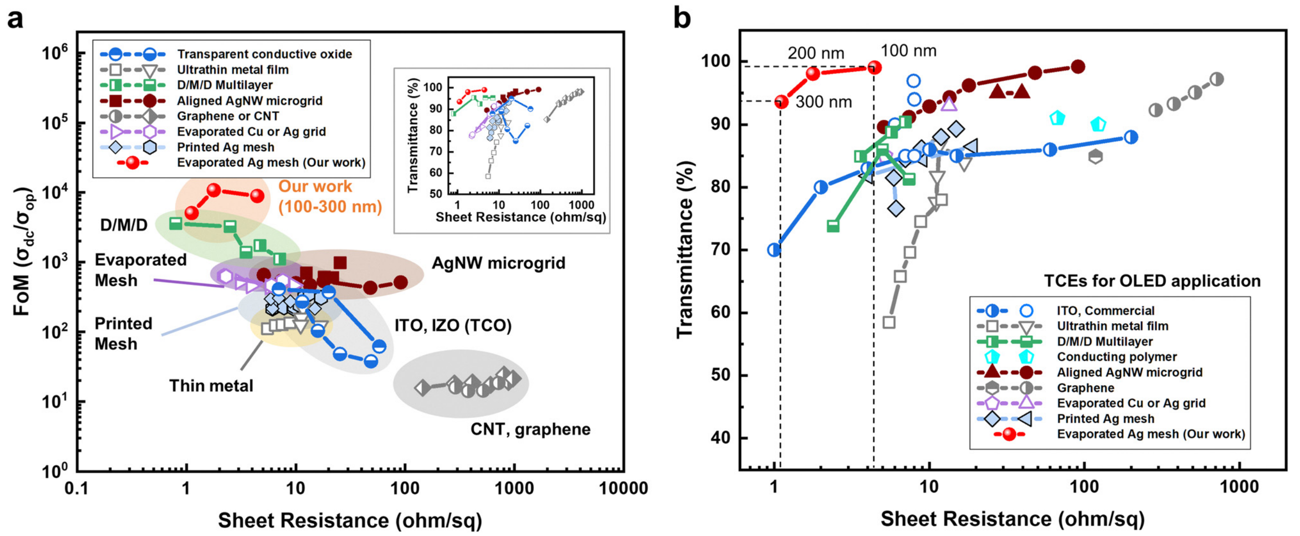

Fig. 5 Optical and electrical characteristics of the fabricated metal mesh. (a) Comparison of transmittance, sheet resistance, and figure of merits to previous studies with high-performance thin-film transparent electrodes incorporating transparent conductive oxides,[8,48] ultrathin metal films,[49,50] D/M/D multilayers,[51,52] AgNWs,[7,14] graphene,[15] CNTs,[17] evaporated[37,53] or printed[24,26] metal mesh. (b) Comparison of transmittance and sheet resistance to previous studies with the transparent electrode of OLED device applications incorporating ultrathin metal films,[49,50] D/M/D multilayers,[5,54] conducting polymers,[6,13] AgNW,[7,55] graphene,[15,16] evaporated[56,57] or printed[24,25] metal mesh.

alternative to ITO for high-performance transparent thin-film electrodes.

To further evaluate the advantages of our metal mesh electrodes in terms of performance and process compatibility, in Fig. 5b, we compare their transmittance and sheet resistance to those reported in previous studies with transparent electrodes applied to OLED devices, including ultrathin metal films,[49,50] D/M/D multilayers,[5,54] conducting polymers,[6,13] nanomaterials (AgNWs[7,55] or graphene[15,16]), as well as evaporated metal mesh[56,57] or printed metal mesh[24,25] (Table S7). This comparison confirms that our metal mesh electrodes exhibit one of the highest optical transmittance values and the lowest sheet resistance compared to other transparent electrodes previously reported with OLED devices. Moreover, the fabrication method does not involve immersion in electrolyte solutions or organic solvents, thereby eliminating the risk of damaging underlying organic layers during processing. This characteristic demonstrates excellent compatibility with OLED device applications.

### 2.5. Transparent OLED fabrication

Taking advantage of the high transparency and good conductivity of the fabricated metal mesh electrode, transparent OLEDs were demonstrated. Detailed information on the fabrication process is suggested in the Experimental section and SI (Fig. S13). Fig. 6a shows the example optical images of the fabricated OLED device during electroluminescence (EL) emission from the top and bottom side, applying a current bias of 1 mA. The top cathode of the example device was a metal mesh electrode with a thickness of 100 nm, a linewidth of 4.4 μm, and a line spacing of 47 μm. The background letters beneath the device were visible through the pixel from both the top and bottom sides. In the ON state, emitted light was extracted from both sides of the device, through the metal mesh cathode at the top and through the ITO anode at the bottom. Enlarged optical microscopy images reveal the emission patterns, including lightened edges of the mesh patterns from the top view, and full mesh patterns from the bottom view. Also, Fig. 6b presents the example transmittance data of a fabricated device in the visible light region, compared with the reference device with a 20 nm thin Ag top electrode. The thickness of the thin Ag electrode is optimized by measuring their transmittance and sheet resistance (Table S8 and Fig. S14). At a reference wavelength of 550 nm, the OLED device with the metal mesh electrode showed 65.9% transmittance and the OLED device with the 20 nm Ag electrode showed only 25.5% transmittance (Fig. 6b). Notably, the OLEDs with the example metal mesh electrode demonstrated over 2.5 times higher transmittance than those with the 20 nm Ag electrode, highlighting the superior transparency of the mesh structure.

Moreover, the current density–voltage–luminance ($J$–$V$–$L$) characteristics, device efficiencies, and electroluminescent (EL) spectra of the example OLED device with the metal mesh top electrodes were compared with those of a reference device employing non-patterned 20 nm Ag, as presented in Fig. 7a–c. Both devices had identical bottom ITO electrodes and the OLED layer configuration, and the luminance and EL spectra of the OLED devices were measured from the bottom-emission side. Note that the areal fill factor was not considered in the average current density and the average luminance measurements. The (average) current density was calculated based on the full pixel area, and the (average) luminance was measured using a 1° measuring angle, corresponding to the circle (measurement area) annotated in Fig. S15. The OLED device with metal mesh exhibited a lower average current density and average luminance compared to the reference device (Fig. 7a); however, at a given average current density, the OLED device with metal mesh showed higher average luminance compared to the reference device (inset of Fig. 7a). At an average current density of 30 mA cm$^{-2}$, the corresponding luminance values were 2679 cd m$^{-2}$ at 11 V for the reference device, and 3257 cd m$^{-2}$ at 14 V for the OLED device with the metal mesh.

These trends are further reflected in the device efficiencies presented in Fig. 7b. It can be noted that the current efficiency is effectively equivalent to the local current efficiency within the metal mesh region using the following equation (eqn (2)),

$$\text{Current efficiency} = \frac{L_{\text{avg}}}{J_{\text{avg}}} = \frac{L_{\text{avg}} \times \dfrac{100\ (\%)}{\text{FF}\ (\%)}}{J_{\text{avg}} \times \dfrac{100\ (\%)}{\text{FF}\ (\%)}} = \frac{L_{\text{local}}}{J_{\text{local}}} \tag{2}$$

where $J_{\text{local}}$, $J_{\text{avg}}$, $L_{\text{local}}$, $L_{\text{avg}}$, and FF represent the local current density, average current density, local luminance, average luminance, and areal fill factor of the metal mesh pattern, respectively. The optical reflectance data measured with various

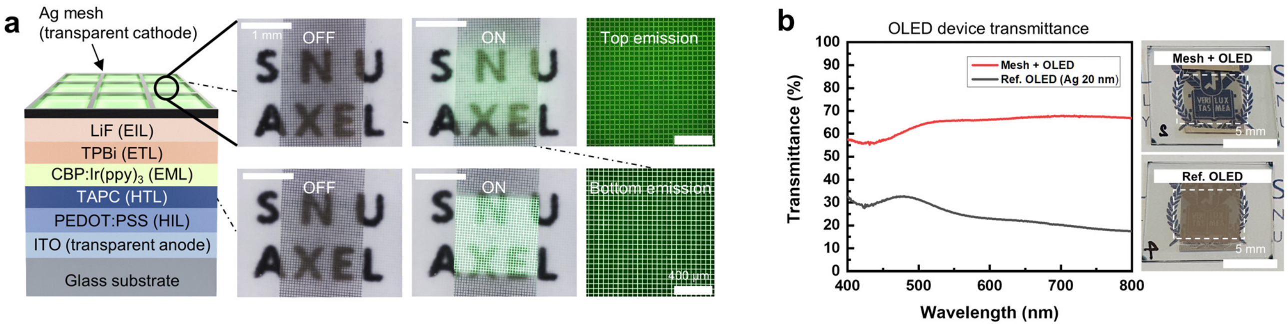

Fig. 6 Transparent OLED with the top metal mesh cathode. (a) Emission image at the top side and bottom side. (b) OLED device transmittance.

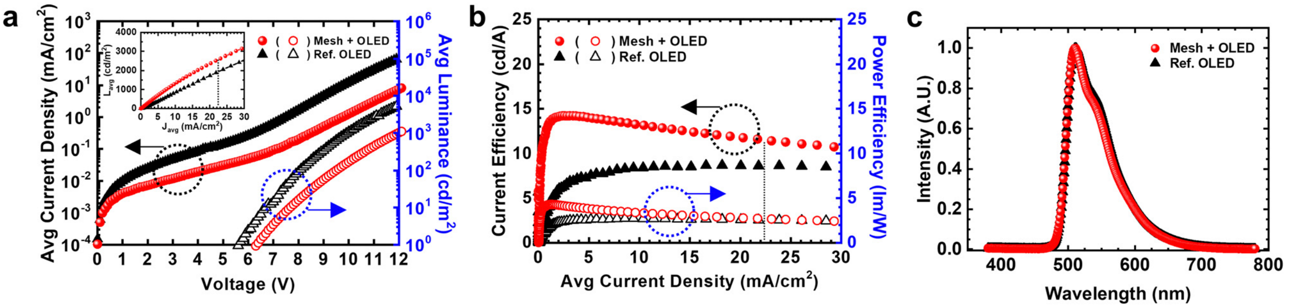

Fig. 7 Transparent OLED with the top metal mesh cathode. (a) *J*–*V*–*L* graph (inset: *J*–*L* graph), (b) current and power efficiencies and (c) EL spectra.

Table 1 OLED device characteristics with different top cathodes

| | $V_{\text{on,avg}}$ (V) | $V_{\text{on,local}}$ (V) | CE (cd A$^{-1}$)/PE (lm W$^{-1}$)/EQE (%) Maximum | CE (cd A$^{-1}$)/PE (lm W$^{-1}$)/EQE (%) at 1000 cd m$^{-2}$ | Average $L$ (cd m$^{-2}$) At $J_{\text{avg}}$ = 30 mA cm$^{-2}$ | $\lambda_{\text{max}}$ (nm) | CIE ($x$, $y$) |
|---|---|---|---|---|---|---|---|
| Mesh + OLED | 6.4 | 5.7 | 14.2/4.3/4.2 | 13.6/3.6/4.0 | 3257 (14 v) | 511 | (0.30, 0.62) |
| Ref. OLED | 5.7 | | 8.7/2.7/2.5 | 8.5/2.7/2.4 | 2679 (11 v) | 511 | (0.30, 0.62) |

$V_{\text{on,avg}}$: turn-on voltage (V) at average luminance = 1 cd m$^{-2}$, $V_{\text{on,local}}$: turn-on voltage (V) at local luminance = 1 cd m$^{-2}$

thicknesses of deposited Ag film are provided in Fig. S16 and summarized in Table S9. The top electrode of the reference device (non-pattern 20 nm Ag) exhibited a sheet resistance of 2.0 Ohm sq$^{-1}$, and an optical reflectance of 53.0%. In contrast, the mesh electrode of the OLED device with metal mesh showed a slightly higher sheet resistance of 2.2 Ohm sq$^{-1}$, but a substantially higher optical reflectance of 97.4% in the mesh-patterned region, due to the thicker Ag layer (100 nm). Higher reflectance from the top electrode leads to more emitted light being reflected downward and extracted through the ITO, thereby enhancing device luminance and overall device efficiency. Thus, despite having comparable sheet resistance, most of the emitted light in the OLED device with the metal mesh was expected to be reflected toward the bottom side; in contrast, only about half was expected to be extracted in the reference device. Consequently, the current efficiency of the OLED device with metal mesh exhibits 63% enhanced maximum current efficiency (60% enhanced current efficiency at 1000 cd m$^{-2}$) compared to the reference device, as shown in Fig. 7b. These results are summarized in Table 1. Furthermore, when considering emissions from both the top and bottom sides, the OLED device with metal mesh exhibited a higher total maximum current efficiency compared to the reference device (Fig. S17 and Table S10).

Based on the average luminance, the reference device exhibited a turn-on voltage of 5.7 V, while the OLED device with metal mesh cathodes turned on at 6.4 V, as shown in Fig. 7a. This shift in turn-on voltage for OLEDs with the mesh cathode is mainly attributed to their lower areal fill factor and localized light emission from the bottom side. The devices reached their average luminance of 1 cd m$^{-2}$ at their turn-on voltages, but their local luminance already exceeded 1 cd m$^{-2}$ at voltages lower than their turn-on voltages (see eqn (2)). To confirm this result, localized *J*–*V*–*L* characteristics and device efficiencies were plotted with the local current density focused on the mesh patterns and the local luminance. The areal fill factor was calculated as the ratio of the emissive area to the entire pixel area for each device, where the area of emission regions was quantitatively extracted from the emission images presented in Fig. S15. As shown in Fig. S18, the OLED device with metal mesh was locally turned on at 5.7 V from the bottom side, identical to the reference device.

Moreover, the emission spectra of the OLED device with metal mesh closely resembled that of the reference device, exhibiting green emission with a peak wavelength of 511 nm and CIE 1931 ($x$, $y$) chromaticity coordinates of (0.30, 0.62) (Fig. 7c). Maintaining the original emission spectrum, the OLED with metal mesh can be reliably applied to a display application. In addition, the OLED device with metal mesh electrodes exhibited minimal angular variation, with only negligible differences compared to the reference device (Fig. S19). However, the luminance or device efficiencies of the OLEDs with our metal mesh electrodes still remain relatively modest compared to devices employing other transparent electrodes (Table S11, SI), primarily due to differences in the performance of the respective reference devices. The overall OLED device performance with our metal mesh electrodes is expected to be further improved by utilizing optimized materials and device structures with higher emission efficiencies.

## 3. Conclusions

In conclusion, we have demonstrated a facile and effective method to directly fabricate transparent top metal mesh electrodes on OLEDs using the selective metal deposition behavior guided by elastomeric PVDF–HFP. The resulting mesh electrodes exhibit outstanding optical and electrical performance, including a transmittance of 93.6–99.0%, a sheet resistance of

1.1–4.4 Ohm sq$^{-1}$, and a maximum figure of merit exceeding $10^4$ at 200 nm thickness. This performance is among the highest reported for transparent electrodes with sub-micrometer metal thickness. Furthermore, the process eliminates the need for lamination or exposure to solvents or electrolyte solutions, making it highly compatible with organic optoelectronic devices. This strategy provides a promising route toward scalable fabrication of high-performance transparent electrodes without compromising the integrity of underlying device layers. As a result, the fabricated transparent OLED with a top metal mesh electrode exhibited higher transmittance and enhanced device efficiency at the same time compared to the reference device with a 20 nm semitransparent Ag top electrode.

## 4. Experimental

### 4.1. Materials

Extra pure grade acetone and isopropyl alcohol (IPA) were purchased from Daejung Chemicals & Metals (Korea) and were used for cleaning solvents without additional purification. ITO coated glass was purchased from AMG (Korea). SYLGARD 184 Silicone Elastomer (Dow) was used as the PDMS prepolymer. Elastomeric PVDF–HFP (DAI-EL G-8002) was obtained from Daikin Industries. PGMEA (>99.5%), 1,3,5-triallyl-1,3,5-triazine-2,4,6(1*H*,3*H*,5*H*)-trione (triallyl isocyanurate, TAIC), benzoyl peroxide (BPO, Luperox A75), and FOTS were purchased from Sigma-Aldrich. Elastomeric PVDF–HFP was mixed with BPO and TAIC at a weight ratio of 20 : 1 : 1, and was dissolved in PGMEA to obtain the e-PVDF–HFP ink.[37] Poly(3,4-ethylenedioxythiophene)-poly(styrenesulfonate) (PEDOT:PSS, CLEVIOS P VP AI4083) was purchased from Heraeus. 1,1-Bis[4-[*N*,*N*-di(*p*-tolyl)amino]phenyl]cyclohexane (TAPC), 4,4′-bis(9*H*-carbazol-9-yl)biphenyl (CBP), tris(2-phenylpyridinato)iridium(III) (Ir(ppy)$_3$), and 1,3,5-tris(1-phenyl-1*H*-benzimidazol-2-yl)benzene (TPBi) were purchased from Tokyo Chemical Industry. Lithium fluoride (LiF, 3–6 mmpcs, 99.9%) and Ag granule (3–5 mm, 99.99%) were purchased from Taewon Scientific (Korea). UV resin (XNR5570) was purchased from Nagase ChemteX Corporation.

### 4.2. Metal mesh electrode fabrication

A pre-patterned silicon master mold was used after FOTS vapor deposition to facilitate demolding. The PDMS prepolymer was spin-coated on the pre-patterned Si master mold at 300 rpm for 60 s after sufficiently removing air bubbles by vacuum degassing, followed by thermal curing on a hot plate at 120 °C for 1 hour. After curing, a cured PDMS micropillar replica was gently peeled off from the master mold. As a target substrate, bare glass was cleaned with acetone and IPA in an ultrasonic bath, followed by drying in a convection oven at 100 °C for 1 hour. A PDMS micropillar replica stamp was placed on a carrier glass. To overcome its hydrophobic property, the PDMS stamp surface was treated with air plasma (CUTE, Femto Science) before spin-coating. Metal-vapor-desorption ink of elastomeric PVDF–HFP was spin-coated on the stamp at 4000 rpm for 60 s. After coating, the stamp with spin-coated e-PVDF–HFP was detached from the carrier glass and attached onto the target surface without any supporting film. After ensuring conformal contact with the target surface, the stamp was detached from the target surface using an automatic stage at a controlled speed (Fig. S20, SI). After sufficiently drying residual solvents on the target surface, the substrate with patterned e-PVDF–HFP film was placed in a vacuum thermal evaporator without any additional mask. Thermal evaporation was carried out below the vacuum level of $10^{-6}$ torr. Ag was thermally evaporated using a tungsten boat, to a thickness of 100 nm unless stated otherwise.

### 4.3. Transparent OLED fabrication

Phosphorescent green OLEDs were fabricated on a glass substrate incorporating ITO as the bottom anode and metal mesh electrodes as the top cathode. As a substrate, a glass with a patterned ITO anode was cleaned with acetone and IPA in an ultrasonic bath, followed by drying in a convection oven at 100 °C for 1 hour. The substrate was cleaned in a UV-O$_3$ cleaner (AH1700, Ahtech LTS) for 5 min before use. The hole injection layer of PEDOT:PSS was spin-coated at 2000 rpm for 60 s and dried at 120 °C for 30 min. Then, the substrate was placed in a vacuum thermal evaporator. The hole transport layer of TAPC, the emitting layer consisting of CBP as the host and Ir(ppy)$_3$ as the guest (8%), and the electron transport layer of TPBi were successively deposited at a rate of 1.0 Å s$^{-1}$ using zirconium dioxide crucibles, followed by electron injection layer (LiF) deposition at a rate of 0.1 Å s$^{-1}$ using a tungsten boat without breaking the vacuum. After deposition, the substrate was removed from the vacuum chamber and placed in a connected N$_2$-filled glovebox without exposure to ambient conditions. Then, the PDMS micropillar stamp with spin-coated e-PVDF–HFP was moved into the glovebox, followed by the transfer printing process mentioned above. The OLED device without a top electrode served as the target surface for transfer printing. After transfer printing, the sample was moved into a thermal evaporator for Ag deposition at a rate of 2.0 Å s$^{-1}$ using a tungsten boat. Ag was deposited through a metal mask, simultaneously forming the transparent metal mesh electrode with bus line patterns. Finally, the fabricated transparent OLED was encapsulated with a glass lid and a UV-curable epoxy in a nitrogen atmosphere. For transmittance measurement, non-patterned ITO coated glass was used in place of the patterned ITO glass.

### 4.4. Characterization and measurements

*J*–*V*–*L* characteristics and the emission spectrum of the OLED were measured using a spectrometer (CS-2000, Konica Minolta) with a source meter (Keithley 2400, Tektronix) and a source measure unit (Keithley 236, Tektronix) by sweeping the voltage at an interval of 0.1 V. The optical images were obtained using two digital microscopes, DSX510 (Olympus) and HR-1020E (Hirox). For OLED emission images, a source meter (Keithley 2400, Tektronix) was used simultaneously to apply electrical bias. The photographs of the samples were taken using a Galaxy S10 5G smartphone. The surface images of the metal mesh electrode were captured by field emission scanning electron microscopes (FE-SEM), S-4800 (Hitachi). The elemental mapping and line scan analysis of atomic components were carried out using FE-SEM (JSM-IT800SHL, JEOL) equipped with an energy-dispersive X-ray spectroscopy (EDS) detector. Surface morphology was observed using an AFM (Cypher S, Oxford Instruments) with an AC160TSA-R3 AFM probe (Oxford Instruments, with a nominal spring constant of 26 N $m^{-1}$, a resonance frequency of 300 kHz, and a tip radius of 7 nm). The scan resolution was set to 256 × 256 pixels with a scan rate of 0.6 Hz. The data were analyzed with the scanning probe microscopy data processing software Gwyddion 2.70. The contact angle of the ink was measured with a contact angle analyzer (Phoenix-MT, SEO). The ink containing 5 wt% e-PVDF–HFP was used for the contact angle measurement. The work of adhesion of the ink to the stamp was calculated using the measured contact angle and the surface tension of the ink[38] by the Young-Dupré equation,[58] $W_a = \gamma_L(1 + \cos\theta)$, where $W_a$, $\gamma_L$ and $\theta$ are the work of adhesion of the liquid to the solid, surface tension of the liquid, and the contact angle, respectively. For measuring geometrical parameters or areal coverage, captured optical images were analyzed using an ImageJ plugin. The transmittance and the reflectance were measured using a UV/Vis spectrometer, Lambda 35 (PerkinElmer). The transmission haze was analyzed by a UV/Vis spectrometer with an integrating sphere (V-770, Jasco). The sheet resistance was measured using four-point probes spaced 1 mm apart and connected to a source meter (Keithley 2400, Tektronix)

## Conflicts of interest

There are no conflicts to declare.

## Data availability

All data supporting this study are provided as supplementary information (SI) accompanying this paper. Supplementary information (SI) is available. See DOI: https://doi.org/10.1039/d5mh02144h.

## Acknowledgements

This research was supported by the Commercialization Promotion Agency for R&D Outcomes (COMPA) funded by the Ministry of Science and ICT (MSIT) (RS-2025-02316237). This research was also supported by the National Research Foundation of Korea (NRF) funded by the Korea government (MSIT) (RS-2024-00416978). This research was also supported by the Basic Science Research Program through the National Research Foundation of Korea (NRF) funded by the Ministry of Education (RS-2025-25396400).

## References

1 S. M. Lee, J. H. Kwon, S. Kwon and K. C. Choi, *IEEE Trans. Electron Devices*, 2017, **64**, 1922–1931.
2 G. Huseynova, J.-H. Lee, Y. H. Kim and J. Lee, *Adv. Opt. Mater.*, 2021, **9**, 2002040.
3 M. Althumayri, R. Das, R. Banavath, L. Beker, A. M. Achim and H. Ceylan Koydemir, *Adv. Sci.*, 2024, **11**, 2405099.
4 K. Ellmer, *Nat. Photonics*, 2012, **6**, 809–817.
5 M. Kim, C. Lim, D. Jeong, H.-S. Nam, J. Kim and J. Lee, *Org. Electron.*, 2016, **36**, 61–67.
6 S. Kee, N. Kim, B. Park, B. S. Kim, S. Hong, J.-H. Lee, S. Jeong, A. Kim, S.-Y. Jang and K. Lee, *Adv. Mater.*, 2018, **30**, 1703437.
7 X. Feng, L. Wang, Y. Y. S. Huang, Y. Luo, J. Ba, H. H. Shi, Y. Pei, S. Zhang, Z. Zhang, X. Jia and B. Lu, *ACS Appl. Mater. Interfaces*, 2022, **14**, 39199–39210.
8 H. Kim, J. S. Horwitz, G. Kushto, A. Piqué, Z. H. Kafafi, C. M. Gilmore and D. B. Chrisey, *J. Appl. Phys.*, 2000, **88**, 6021–6025.
9 H. H. Yu, S.-J. Hwang, M.-C. Tseng and C.-C. Tseng, *Opt. Commun.*, 2006, **259**, 187–193.
10 M. Mazur, D. Kaczmarek, J. Domaradzki, D. Wojcieszak, S. Song and F. Placido, *Presented in part at The Eighth International Conference on Advanced Semiconductor Devices and Microsystems*, Slovakia, 2010.
11 H. Cho, G. H. Kim, W.-J. Lee and Y.-H. Kim, *ETRI J.*, 2025, **47**, 1115–1124.
12 H. Lei, M. Wang, Y. Hoshi, T. Uchida, S. Kobayashi and Y. Sawada, *Appl. Surf. Sci.*, 2013, **285**, 389–394.
13 M. Zhang, S. Höfle, J. Czolk, A. Mertens and A. Colsmann, *Nanoscale*, 2015, **7**, 20009–20014.
14 K. Zhang, L. Meng, M. Zhang, Y. Li, L. Jiang and H. Liu, *Adv. Funct. Mater.*, 2024, **34**, 2308468.
15 B. Kulyk, J. C. Germino, D. Gaspar, A. J. S. Fernandes, J. Deuermeier, A. F. Carvalho, A. F. da Cunha, L. M. N. Pereira, L. Pereira and F. M. Costa, *J. Mater. Chem. C*, 2025, **13**, 5855–5864.
16 J.-H. Chang, W.-H. Lin, P.-C. Wang, J.-I. Taur, T.-A. Ku, W.-T. Chen, S.-J. Yan and C.-I. Wu, *Sci. Rep.*, 2015, **5**, 9693.
17 I. Jeon, J. Yoon, U. Kim, C. Lee, R. Xiang, A. Shawky, J. Xi, J. Byeon, H. M. Lee, M. Choi, S. Maruyama and Y. Matsuo, *Adv. Energy Mater.*, 2019, **9**, 1901204.
18 X. Lu, Y. Zhang and Z. Zheng, *Adv. Electron. Mater.*, 2021, **7**, 2001121.
19 Z. B. Wang, M. G. Helander, J. Qiu, D. P. Puzzo, M. T. Greiner, Z. M. Hudson, S. Wang, Z. W. Liu and Z. H. Lu, *Nat. Photonics*, 2011, **5**, 753–757.
20 N. P. Sergeant, A. Hadipour, B. Niesen, D. Cheyns, P. Heremans, P. Peumans and B. P. Rand, *Adv. Mater.*, 2012, **24**, 728–732.
21 A. Lorusso, S. Masi, C. Triolo, F. Mariano, S. Muia, A. Cannavale, Y. Duan, M. Anni, M. L. De Giorgi, S. Patané, O. Selmi, I. Mora-Seró, S. De Leo and M. Mazzeo, *ACS Energy Lett.*, 2024, **9**, 1923–1931.
22 H. B. Lee, W.-Y. Jin, M. M. Ovhal, N. Kumar and J.-W. Kang, *J. Mater. Chem. C*, 2019, **7**, 1087–1110.

23 V. H. Nguyen, D. T. Papanastasiou, J. Resende, L. Bardet, T. Sannicolo, C. Jiménez, D. Muñoz-Rojas, N. D. Nguyen and D. Bellet, *Small*, 2022, **18**, 2106006.

24 L.-Q. Yao, Y. Qin, X.-C. Li, Q. Xue, F. Liu, T. Cheng, G.-J. Li, X. Zhang and W.-Y. Lai, *InfoMat*, 2023, **5**, e12410.

25 S. Park, J. T. Lim, W.-Y. Jin, H. Lee, B.-H. Kwon, N. S. Cho, J.-H. Han, J.-W. Kang, S. Yoo and J.-I. Lee, *ACS Photonics*, 2017, **4**, 1114–1122.

26 Z. Jiang, K. Fukuda, X. Xu, S. Park, D. Inoue, H. Jin, M. Saito, I. Osaka, K. Takimiya and T. Someya, *Adv. Mater.*, 2018, **30**, 1707526.

27 Y. Li, L. Meng, Y. Yang, G. Xu, Z. Hong, Q. Chen, J. You, G. Li, Y. Yang and Y. Li, *Nat. Commun.*, 2016, **7**, 10214.

28 H. Yoon, S. Jeong, B. Lee, D. Kim, J. Park and Y. Hong, *Flex. Print. Electron.*, 2023, **8**, 015005.

29 Y. S. Oh, J. Lee, D. Y. Choi, H. Lee, K. Kang, S. Yoo, I. Park and H. J. Sung, *Sci. Rep.*, 2020, **10**, 6782.

30 H. J. Lee, B.-H. Kim, A. V. Takaloo, K. R. Son, T. D. Dongale, K. M. Lim and T. G. Kim, *Adv. Opt. Mater.*, 2021, **9**, 2002010.

31 F.-S. Yi, Y.-G. Bi, X.-M. Gao, X.-M. Wen, X.-L. Zhang, Y.-F. Liu, D. Yin, J. Feng and H.-B. Sun, *Org. Electron.*, 2020, **87**, 105960.

32 S. Wang, J. Xu, W. Wang, G.-J. N. Wang, R. Rastak, F. Molina-Lopez, J. W. Chung, S. Niu, V. R. Feig, J. Lopez, T. Lei, S.-K. Kwon, Y. Kim, A. M. Foudeh, A. Ehrlich, A. Gasperini, Y. Yun, B. Murmann, J. B. H. Tok and Z. Bao, *Nature*, 2018, **555**, 83–88.

33 J. Cai, M. Zhang, Z. Sun, C. Zhang, C. Liang, A. Khan, X. Ning, H. Ge, S.-P. Feng and W.-D. Li, *J. Mater. Chem. C*, 2019, **7**, 4363–4373.

34 A. Khan, S. Lee, T. Jang, Z. Xiong, C. Zhang, J. Tang, L. J. Guo and W.-D. Li, *Small*, 2016, **12**, 3021–3030.

35 S. Varagnolo, J. Lee, H. Amari and R. A. Hatton, *Mater. Horiz.*, 2020, **7**, 143–148.

36 S. Varagnolo, K.-W. Park, J.-K. Lee and R. A. Hatton, *J. Mater. Chem. C*, 2020, **8**, 13453–13457.

37 P. Bellchambers, C. Henderson, S. Abrahamczyk, S. Choi, J.-K. Lee and R. A. Hatton, *Adv. Mater.*, 2023, **35**, 2300166.

38 S. Jeong, H. Yoon, L. F. Michalek, G. Kim, J. Kim, J. Seo, D. Kim, H. Park, B. Lee and Y. Hong, *Nat. Commun.*, 2024, **15**, 7209.

39 T. Tsujioka, Y. Sesumi, R. Takagi, K. Masui, S. Yokojima, K. Uchida and S. Nakamura, *J. Am. Chem. Soc.*, 2008, **130**, 10740–10747.

40 R. Takagi, K. Masui, S. Nakamura and T. Tsujioka, *Appl. Phys. Lett.*, 2008, **93**, 213304.

41 T. Tsujioka and M. Dohi, *Appl. Phys. Express*, 2014, **7**, 071602.

42 T. Tsujioka and H. Kusaka, *Adv. Mater. Interfaces*, 2022, **9**, 2201096.

43 Z. Wang, Y.-l Chang, Q. Wang, Y. Zhang, J. Qiu and M. G. Helander, *Inf. Display*, 2021, **37**, 16–21.

44 S. K. Kim, K.-S. Kim, H.-U. Park, J. Y. Kim, D. K. Kim, S.-H. Kim, J.-H. Baek, J.-J. Kim, R. Pode and J. H. Kwon, *J. Ind. Eng. Chem.*, 2022, **114**, 213–220.

45 J. Seo, J. Yoon, G. Kim, H. Cho, D. Jang, H. Yoon, S. Choi and Y. Hong, *ACS Appl. Electron. Mater.*, 2023, **5**, 2769–2780.

46 S. Bhattacharya, A. Datta, J. M. Berg and S. Gangopadhyay, *J. Microelectromechanical Syst.*, 2005, **14**, 590–597.

47 M. Dressel and G. Grüner, *Electrodynamics of Solids: Optical Properties of Electrons in Matter*, Cambridge University Press, Cambridge, 2002.

48 Z. Ying, Y. Zhu, X. Feng, J. Xiu, R. Zhang, X. Ma, Y. Deng, H. Pan and Z. He, *Adv. Mater. Interfaces*, 2021, **8**, 2001604.

49 D. Yin, Z.-Y. Chen, N.-R. Jiang, Y.-F. Liu, Y.-G. Bi, X.-L. Zhang, W. Han, J. Feng and H.-B. Sun, *Org. Electron.*, 2020, **76**, 105494.

50 E.-y Choi, S.-C. Kang, K. Kim, S.-H. Lee, J.-B. Kim and J.-K. Song, *Light: Sci. Appl.*, 2025, **14**, 62.

51 H. Ferhati and F. Djeffal, *J. Comput. Electron.*, 2020, **19**, 815–824.

52 D. R. Sahu, S.-Y. Lin and J.-L. Huang, *Appl. Surf. Sci.*, 2006, **252**, 7509–7514.

53 P. Bellchambers, S. Varagnolo, C. Maltby and R. A. Hatton, *ACS Appl. Energy Mater.*, 2021, **4**, 4150–4155.

54 K.-H. Choi, H.-J. Nam, J.-A. Jeong, S.-W. Cho, H.-K. Kim, J.-W. Kang, D.-G. Kim and W.-J. Cho, *Appl. Phys. Lett.*, 2008, **92**, 223302.

55 R. E. Triambulo, H.-G. Cheong and J.-W. Park, *Org. Electron.*, 2014, **15**, 2685–2695.

56 X. Huang, F. Zhang, Y. Liu and J. Leng, *ACS Appl. Mater. Interfaces*, 2020, **12**, 23236–23243.

57 P. Liu, B. Huang, L. Peng, L. Liu, Q. Gao and Y. Wang, *Sci. Rep.*, 2022, **12**, 20494.

58 M. E. Schrader, *Langmuir*, 1995, **11**(9), 3585–3589.